Homodyne detection in ghost imaging with thermal light

Pengli Zhang, Wenlin Gong, Xia Shen, and Shensheng Han*
Key Laboratory for Quantum Optics and Center for Cold Atom Physics, Shanghai Institute of Optics and Fine Mechanics, Chinese Academy of Sciences, Shanghai 201800, China

Rong Shu
Shanghai Institute of Technical Physics, Shanghai 200083, China
(Received 22 June 2009; published 17 September 2009)

Homodyne detection is a well-known technique in measuring phase-dependent properties of optical radiation. We apply balanced homodyne detection to ghost imaging with thermal light, and analyze how to obtain the amplitude and phase information about an object by optimizing the optical setups and controlling the local oscillators. Compared with ghost imaging using direct detection, the homodyne detection scheme is very sensitive to phase changes of optical fields so that it can be used to image a pure phase object. The analytical results are backed up by numerical simulations based on statistical optics.

DOI: 10.1103/PhysRevA.80.033827 PACS number(s): 42.50.Ar, 42.30.Va, 42.30.Wb

I. INTRODUCTION

In general, optical radiation can be measured either by direct detection, in which the distribution of the light intensity falls directly on a photodetector, or by homodyne detection [1,2], in which the incident optical field is mixed with a local oscillator (LO) of the same frequency before detection. Compared with direct detection that only provides information about the mean photon number (light intensity) [3], homodyne detection can give access to the quadrature components of the optical field, which has been widely used in studies and applications of squeezed states in quantum optics [4–7].

Ghost imaging is a novel technique that forms an object image or its diffraction pattern (Fourier transform) by measuring two correlated optical fields [8–16]. Traditionally, the two correlated fields are measured with direct detection, and performing the intensity correlation will generate a background term [9,10], which involves no information about the object and usually need to be subtracted to improve the visibility of the image. In this paper, a balanced homodyne detection scheme for ghost imaging with thermal light is presented in detail. By using balanced homodyne detection, the correlation function of the optical fields becomes second order instead of fourth order, and the background term encountered in direct detection schemes [9–13] can be removed. The optical setups of the homodyne detection scheme and the detailed analytical calculations are shown in Sec. II. The numerical results based on statistical optics are contained in Sec. III and the paper is summarized in Sec. IV.

II. SYSTEM SETUPS AND ANALYTICAL RESULTS

A balanced homodyne detection scheme of ghost imaging with thermal light is depicted in Fig. 1. A 50/50 nonpolarizing beam splitter (BS) divides quasimonochromatic thermal light with a center wavelength λ into two beams propagating through the test arm and the reference arm, respectively. An object is put immediately after the BS in the test arm and a lens is located at focal distance f from the object as well as to the detection plane P_1, which constitutes a so-called f-f setup [10]. In the reference arm, another lens of focal length f is placed at d_1 from the BS and d_2 from the detection plane P_2. The light fields $E_i(\vec{x}_i,t)$ at the detection planes $P_i(i=1,2)$ are related to the field $E_0(\vec{x}_0,t)$ at the plane P_0 by the Fresnel diffraction integral [17]

$$E_i(\vec{x}_i,t) = \int d\vec{x}_0 E_0(\vec{x}_0,t) h_i(\vec{x}_i,\vec{x}_0), \quad i=1,2, \tag{1}$$

where $h_i(\vec{x}_i,\vec{x}_0)(i=1,2)$ describe the impulse response functions of the test arm and the reference arm, respectively. Two balanced homodyne detectors instead of intensity detectors are used to measured the optical fields at P_i. As shown in

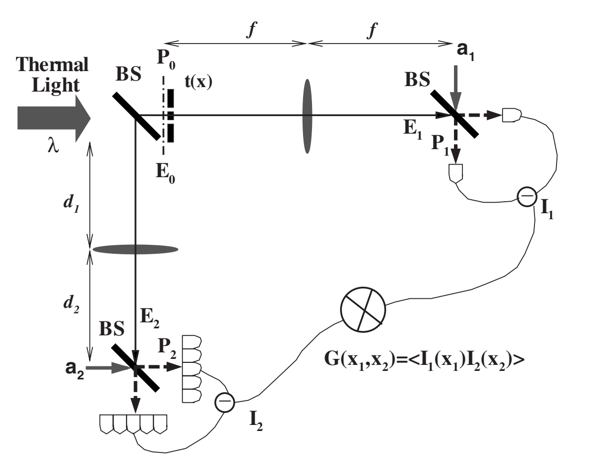

FIG. 1. The homodyne detection scheme for ghost imaging with thermal light, where the test arm contains a fixed f-f setup and two pointlike detectors. The reference arm has the two alternative configurations, $d_1=d_2=f$ and $d_1=d_2=2f$, which can be used to reconstruct the diffraction pattern and image of the object, respectively. BS, 50/50 nonpolarizing beam splitter; f, focal length of the lenses; $t(x)$, the complex transmission function of the object.

*sshan@mail.shcnc.ac.cn

Fig. 1, the input field $E_i(\vec{x}_i,t)$ and an LO $a_i(\vec{x}_i,t)$ combine at a 50/50 beam splitter to give the sum and difference fields $[E_i(\vec{x}_i,t)+a_i(\vec{x}_i,t)]/\sqrt{2}$ and $[E_i(\vec{x}_i,t)-a_i(\vec{x}_i,t)]/\sqrt{2}$, respectively. Then the combined fields are incident on a pair of photodetectors and the output signal I_i is determined by the difference photocurrent between the two photodetectors,

$$I_i(\vec{x}_i,t)=\frac{1}{2}\{|E_i(\vec{x}_i,t)+a_i(\vec{x}_i,t)|^2-|E_i(\vec{x}_i,t)-a_i(\vec{x}_i,t)|^2\}$$
$$=a_i^*(\vec{x}_i,t)E_i(\vec{x}_i,t)+a_i(\vec{x}_i,t)E_i^*(\vec{x}_i,t), \quad (2)$$

where only interference terms between the input field and the LO field survive. In homodyne detection, the LO is at the same center frequency as the input field so that, with quasimonochromatic fields, Eq. (2) no longer has any time dependence,

$$I_i(\vec{x}_i)=|a_i(\vec{x}_i)|\{E_i(\vec{x}_i)e^{-j\phi_i(\vec{x}_i)}+E_i^*(\vec{x}_i)e^{j\phi_i(\vec{x}_i)}\}, \quad (3)$$

where $a_i(\vec{x}_i)$ is treated as a classical coherent field with a phase $\phi_i(\vec{x}_i)$. In Eq. (3), each of the quadrature components of the input field can be obtained by adjusting $\phi_i(\vec{x}_i)$. Thus, intensity fluctuations in homodyne detection directly measure the fluctuations in a quadrature of the input field, which suggests that the desired quadrature components of the transmitted field from the object can be reconstructed through the correlation measurement.

Performing the correlation between the output signals of the two homodyne detectors, I_1 and I_2, we get

$$G(\vec{x}_1,\vec{x}_2)=\langle I_1(\vec{x}_1)I_2(\vec{x}_2)\rangle$$
$$=\{a_1^*(\vec{x}_1)a_2(\vec{x}_2)\langle E_1(\vec{x}_1)E_2^*(\vec{x}_2)\rangle+\text{c.c}$$
$$+a_1(\vec{x}_1)a_2(\vec{x}_2)\langle E_1(\vec{x}_1)E_2(\vec{x}_2)\rangle+\text{c.c}\}, \quad (4)$$

where we have used the fact that $E_i(\vec{x}_i)$ and $a_i(\vec{x}_i)$ are statistically independent of each other. Further, the term $\langle E_1(\vec{x}_1)E_2(\vec{x}_2)\rangle$ in Eq. (4) approaches zero for a thermal field obeying Gaussian statistic [18]. Substituting Eq. (1) into Eq. (4) yields

$$G(\vec{x}_1,\vec{x}_2)=\Bigg\{a_1^*(\vec{x}_1)a_2(\vec{x}_2)\int\int d\vec{x}_0 d\vec{x}_0'\Gamma_0(\vec{x}_0,\vec{x}_0')$$
$$\times h_1(\vec{x}_1,\vec{x}_0)h_2^*(\vec{x}_2,\vec{x}_0')+\text{c.c}\Bigg\}, \quad (5)$$

where $\Gamma_0(\vec{x}_0,\vec{x}_0')=\langle E_0(\vec{x}_0)E_0^*(\vec{x}_0')\rangle$ is the autocorrelation function of the thermal field $E_0(\vec{x}_0)$ at P_0.

For the specific optical paths shown in Fig. 1. The test arm contains the f-f setup and its impulse response function can be expressed as [17]

$$h_{1,f}(\vec{x}_1,\vec{x}_0)=\frac{e^{jk\cdot 2f}}{j\lambda f}t(\vec{x}_0)\exp\left(-j\frac{k}{f}\vec{x}_0\cdot\vec{x}_1\right), \quad (6)$$

where $t(\vec{x})$ denotes the complex transmission function of the object and $e^{jk\cdot 2f}$ is a constant phase delay associated with the axial propagation distance. Note that all constant phase factors have been retained in the analysis, which are crucial for a phase-sensitive measurement.

In the reference arm, there are two alternative configurations, $d_1=d_2=f$ and $d_1=d_2=2f$, which can be used to obtain the diffraction pattern and image of the object, respectively. When $d_1=d_2=f$, the reference arm also contains an f-f setup and the impulse response function is

$$h_{2,f}(\vec{x}_2,\vec{x}_0)=\frac{e^{jk\cdot 2f}}{j\lambda f}\exp\left(-j\frac{k}{f}\vec{x}_0\cdot\vec{x}_2\right). \quad (7)$$

Assuming that thermal source is fully spatially incoherent and the intensity distribution is uniform with a constant I_0, $\Gamma_0(\vec{x}_0,\vec{x}_0')$ can be represented by a delta function,

$$\Gamma_0(\vec{x}_0,\vec{x}_0')=I_0\delta(\vec{x}_0-\vec{x}_0'). \quad (8)$$

Inserting Eqs. (6)–(8) into Eq. (5), after calculation, we have

$$G_f(\vec{x}_1,\vec{x}_2)=\frac{I_0}{(\lambda f)^2}|a_1^*(\vec{x}_1)a_2(\vec{x}_2)|$$
$$\times\{\tilde{T}[(\vec{x}_1-\vec{x}_2)k/f]e^{j\Delta\phi_f(\vec{x}_1,\vec{x}_2)}+\text{c.c}\}, \quad (9a)$$

$$\Delta\phi_f(\vec{x}_1,\vec{x}_2)\equiv\phi_2(\vec{x}_2)-\phi_1(\vec{x}_1), \quad (9b)$$

where $\tilde{T}(\vec{q})$ is the Fourier transform of $t(\vec{x})$ and $\Delta\phi_f(\vec{x}_1,\vec{x}_2)$ accounts for the phase difference of the two LOs. To extract the desired quadrature components of $\tilde{T}(\vec{q})$, the spatial dependence of the modulus $|a_1^*(\vec{x}_1)a_2(\vec{x}_2)|$ should be eliminated. In fact, as long as the LOs spatial waists are large enough, $|a_1^*(\vec{x}_1)a_2(\vec{x}_2)|$ can be approximated as constant over the whole detection regions and will not affect the correlation seriously [19]. According to Eq. (9a), we can obtain the quadrature corresponding to the real part of the Fourier transform of the object by setting $\Delta\phi_f(\vec{x}_1,\vec{x}_2)=0$, as well as the quadrature corresponding to the imaginary part by making $\Delta\phi_f(\vec{x}_1,\vec{x}_2)=-\pi/2$.

In the case of $d_1=d_2=2f$, the reference arm is an imaging system ($2f$-$2f$ setup) and the impulse response function has the form

$$h_{2,2f}(\vec{x}_2,\vec{x}_0)=-e^{jk\cdot 4f}\exp\left(j\frac{k}{2f}\vec{x}_2^2\right)\delta(\vec{x}_0+\vec{x}_2). \quad (10)$$

Taking Eqs. (6), (8), and (10) into Eq. (5), we get

$$G_{2f}(\vec{x}_1,\vec{x}_2)=\frac{I_0}{\lambda f}|a_1^*(\vec{x}_1)a_2(\vec{x}_2)|\times\{t(-\vec{x}_2)e^{j\Delta\phi_{2f}(\vec{x}_1,\vec{x}_2)}+\text{c.c}\}, \quad (11a)$$

$$\Delta\phi_{2f}(\vec{x}_1,\vec{x}_2)=\phi_2(\vec{x}_2)-\phi_1(\vec{x}_1)-2kf-k\vec{x}_2^2/2f$$
$$-k\vec{x}_1\cdot\vec{x}_2/f+\pi/2. \quad (11b)$$

Compared with Eq. (9b), besides a constant term $\pi/2$, Eq. (11b) contains three extra terms, $2kf$, $k\vec{x}_2^2/2f$, and $k\vec{x}_1\cdot\vec{x}_2/f$, all of which arise from the asymmetry of the optical paths in the two arms and can be eliminated by optimizing the optical setup. First, $2kf$ is a constant phase introduced by the difference between the axial propagation distance of the two arms, which can be compensated with a phase retarder. Second, the quadratic term $k\vec{x}_2^2/f$ can be canceled by placing a thin planoconvex lens with focal length f immediately before the de-

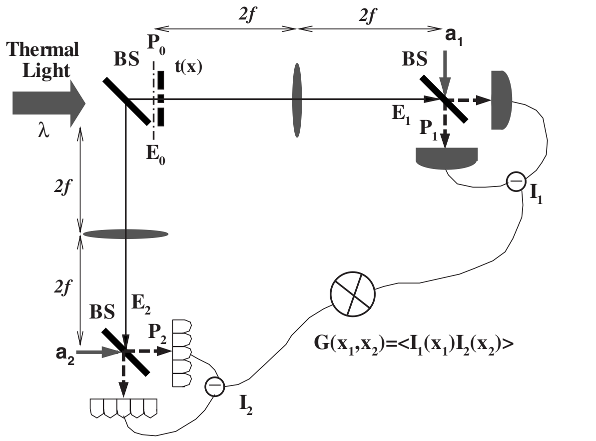

FIG. 2. The homodyne detection scheme for ghost imaging with thermal light, where bucket detectors are used in the test arm and the two arms have the same $2f$-$2f$ setups.

tection plane P_2. Finally, $k\vec{x}_1\cdot\vec{x}_2/f$ is equal to zero when the pointlike detectors in the test arm are fixed at $\vec{x}_1=0$. After the optimization, Eq. (11b) is then rewritten as

$$\Delta\phi_{2f}(\vec{x}_1,\vec{x}_2)=\phi_2(\vec{x}_2)-\phi_1(\vec{x}_1)+\pi/2, \tag{12}$$

which only relies on the phase difference between the two LOs. So, it will be easy to obtain the real and imaginary parts of the complex function $t(\vec{x})$ by choosing $\Delta\phi_{2f}(\vec{x}_1,\vec{x}_2)=0$ and $-\pi/2$, respectively.

In practice, the point detectors in the test arm are difficult to be located at $\vec{x}_1=0$ exactly, so that the term $k\vec{x}_1\cdot\vec{x}_2/f$ in the right of Eq. (11b) is hard to be eliminated completely. A tiny change in the coordinate $\vec{x}_1$ will lead to a tremendous error in the phase exponential because it is multiplied by a very large number k (in the order of 10^7 for the visible light). To overcome the problem, we adopt the symmetrical $2f$-$2f$ imaging setups in the two arms, as shown in Fig. 2. The impulse response function of the reference arm is still given by Eq. (10) and that of the test arm becomes

$$h_{1,2f}(\vec{x}_1,\vec{x}_0)=-e^{jk\cdot 4f}t(\vec{x}_0)\exp\left(j\frac{k}{2f}\vec{x}_1^2\right)\delta(\vec{x}_0+\vec{x}_1). \tag{13}$$

Meanwhile, the point detectors in the test arm have been replaced with the bucket detectors. Applying Eqs. (8), (10), and (13) to Eq. (5) and integrating over $\vec{x}_1$ gives

$$\bar{G}(\vec{x}_2)=\int d\vec{x}_1 G(\vec{x}_1,\vec{x}_2)$$

$$=I_0|a_1^*(\vec{x}_2)a_2(\vec{x}_2)|\{t(-\vec{x}_2)e^{j\Delta\bar{\phi}(\vec{x}_2)}+\text{c.c}\}, \tag{14a}$$

$$\Delta\bar{\phi}(\vec{x}_2)\equiv\phi_2(\vec{x}_2)-\phi_1(\vec{x}_2), \tag{14b}$$

where all phases depending upon the coordinate $\vec{x}_1$ have been cleared up and only the phase difference $\phi_2(\vec{x}_2)-\phi_1(\vec{x}_2)$ plays a key role in the reconstruction of the object image. It is seen that the correlation measurement of $\langle I_1(\vec{x}_1)I_2(\vec{x}_2)\rangle$ can provide the complete information about the object; hence, the homodyne detection scheme can be used to image a pure phase object directly.

III. NUMERICAL RESULTS

The performance of the homodyne detection scheme was checked through numerical simulations of the model described in detail in Ref. [16], which includes the dynamic process of thermal variation, the propagation of optical fields, and the retrieval of images. For most radiation fields without involving nonclassical features of light, such as photon antibunching and squeezed state, statistical properties of the fields can be equally described in classical and quantum theories [20]. There exists a correspondence between the two descriptions if the phase-space representation is employed [21]. Thus, the numerical model based on statistical optics [16] is applicable to the description of a classical thermal source.

In the simulations, the incident thermal field is a circular complex Gaussian random process [17]. A Gaussian laser beam with a waist $\omega_0=800\ \mu$m has been used as the LOs, which have the same center wavelength ($\lambda=0.532\ \mu$m) with the incident field. The focal length of the lenses in the two arms is set as $f=100$ mm.

First of all, we considered the case of the same f-f setups used in the two arms, as shown in Fig. 1. A double slit (slit width $a=100\ \mu$m and center-to-center separation $d=400\ \mu$m) was chosen as the object, whose two-dimensional transmission function corresponds to

$$t(x,y)=\begin{cases}1, & \dfrac{d-a}{2}\le|x-x_0|\le\dfrac{a+d}{2},|y-y_0|\le\dfrac{a+d}{2}\\ 0, & \text{otherwise,}\end{cases} \tag{15}$$

where x_0 and y_0 stand for the central coordinates of the double slit. Its analytical Fourier transform is given by

$$\tilde{T}(q_x,q_y)\propto e^{-jq_xx_0}\cos(q_xd/2)\text{sinc}(q_xa/2)$$
$$\times e^{-jq_yy_0}\,\text{sinc}[q_y(a+d)/2], \tag{16}$$

where $\text{sinc}(\xi)=\sin(\xi)/\xi$, and q_x and q_y represent spatial frequencies kx_2/f and ky_2/f, respectively.

To observe the imaginary part of the object Fourier transform obviously, the center coordinates were set as $x_0=250\ \mu$m and $y_0=250\ \mu$m. After averaging over 10 000 samples in the simulation, the normalized real and imaginary parts of the object Fourier transform are shown in Figs. 3(a) and 3(b). The circles in the Figs. 3(c) and 3(d) represent the profiles of Figs. 3(a) and 3(b) along the x direction, respectively; they are in good agreement with the analytical results $\tilde{T}(q_x,q_y=0)$ [solid lines, Eq. (16)]. Furthermore, by making the inverse Fourier transform of the correlation results in Figs. 3(a) and 3(b), the transmission function of the object can be reconstructed with high quality, as shown in Figs. 3(e) and 3(f). The real part (e) represents the transmission of the object, and the imaginary part (f) is roughly zero, which indicates the object does not alter the phase of the transmitted field.

Second, in the case of the same $2f$-$2f$ setups used in the two arms, as shown in Fig. 2, we selected a pure phase object, defined as

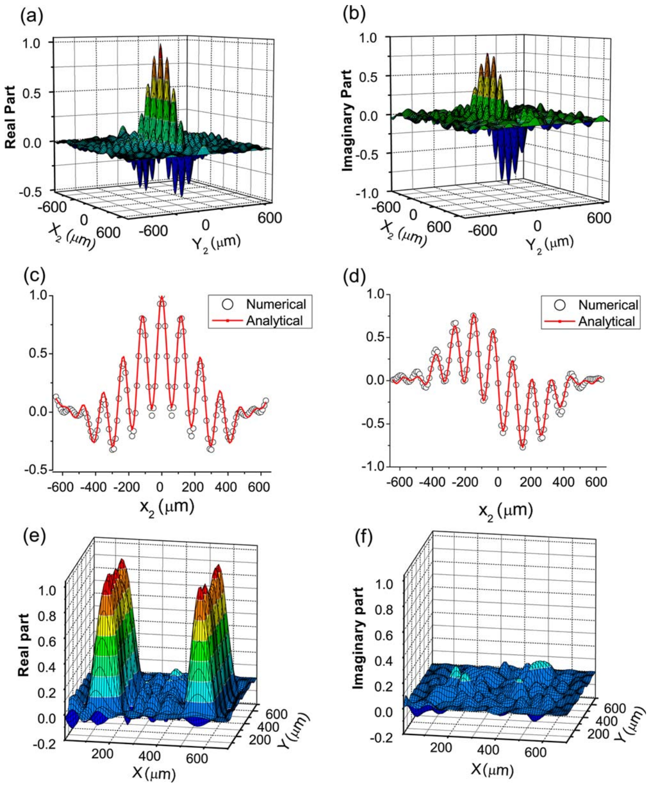

FIG. 3. (Color online) The reconstruction of the object Fourier transform using the same f-f setups in the two arms. (a) and (b) are the normalized real and imaginary parts of the object Fourier transform, respectively, averaged over 10^4 samples. Circles in (c) and (d) are the profiles of figures (a) and (b) alone the x direction, and solid lines correspond to the analytical results $\widetilde{T}(q_x, q_y=0)$ from Eq. (16). (e) and (f) display the real and imaginary parts of the inverse Fourier transform of the correlation results in (a) and (b), respectively.

$$t(x,y) = \exp\left[j\frac{2\pi}{a}\left(x-\frac{a}{2}\right)\right] = \cos\left[\frac{2\pi}{a}\left(x-\frac{a}{2}\right)\right] + j\,\sin\left[\frac{2\pi}{a}\left(x-\frac{a}{2}\right)\right],$$

$$0 \leq x \leq a, \quad 0 \leq y \leq b, \tag{17}$$

where $a=600\ \mu$m and $b=200\ \mu$m are the dimensions of the object in the x and y directions, respectively. By adjusting $\Delta\bar{\phi}(\vec{x}_2)=0$ and $-\pi/2$ in the simulation, the normalized real part [Fig. 4(a)] and imaginary part [Fig. 4(b)] of the transmission function of the pure phase object were reconstructed, respectively. In terms of the acquired data in Figs. 4(a) and 4(b), we retrieved the complete amplitude [Fig. 4(c)] and phase [Fig. 4(d)] of the object transmission function.

At last, we turned to the case of the f-f setup in the test arm and the $2f$-$2f$ setup in the reference arm, as shown in Fig. 1. Apart from the difficulty in experimental implementation, we find that compared to using direct detection, using balanced homodyne detection in this case has greatly improved the convergence rate of the reconstruction of the object image. The qualitative difference of the images reconstructed in the two detection schemes is shown in Fig. 5.

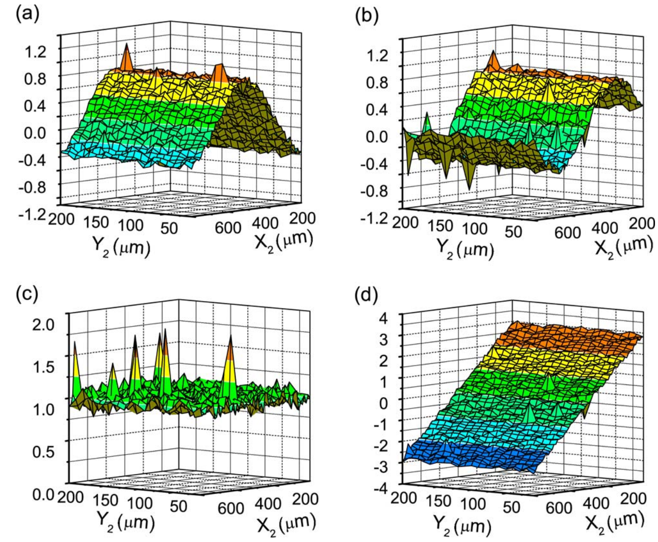

FIG. 4. (Color online) The reconstruction of the pure phase object using the same $2f$-$2f$ setups in the two arms. (a) and (b) display the normalized real and imaginary parts of the object transmittance, respectively; (c) and (d) are the retrieved amplitude and phase of the object transmittance, respectively. 10^4 samples were used.

IV. CONCLUSION

We have demonstrated that balanced homodyne detection can be used to retrieve the full amplitude and phase information of the object image (or diffraction pattern) in ghost imaging with thermal light. A similar homodyne detection scheme based on an entangled source produced by parametric down-conversion (PDC) has been reported in Ref. [19]. For the thermal source, $\langle E_1(\vec{x}_1)E_2(\vec{x}_2)\rangle$ in Eq. (4) is a zero-valued term and $\langle E_1(\vec{x}_1)E_2^*(\vec{x}_2)\rangle$ governs the properties of the correlation function; however, for the PDC source, the result is on the contrary [14]. This difference leads to the conclusion that the homodyne technique with thermal light requires

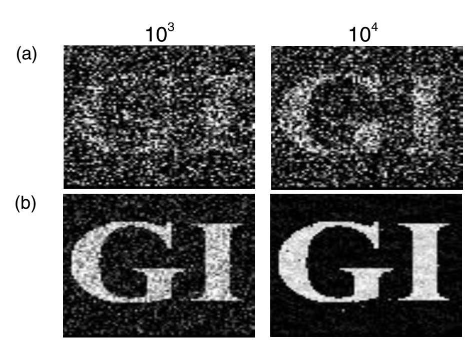

FIG. 5. The qualitative comparison of the object image using the f-f setup in the test arm and the $2f$-$2f$ setup in the reference arm. (a) corresponds to the case using direct intensity detection and (b) is the case using balanced homodyne detection. The sample numbers used in simulations are shown at the top of the images.

a fixed phase difference between the LOs, while that with the PDC source demands "a fixed reference phase" [19]. The other requirement of homodyne detection is that the LO fields should have the same center frequency as the incident thermal field. In most practical applications, a quasimonochromatic thermal field can be easily generated, for example, by illuminating a laser on a slowly rotating ground glass. Thus, it is very convenient to obtain the LOs by taking out some power of the laser before the glass.

It is worthwhile to note that some phase exponentials introduced by light propagation should be treated carefully as homodyne detection is applied to ghost imaging with thermal light. The asymmetry between the two arms usually gives rise to some nuisance phase terms, such as $k\vec{x}_2^2/f$ and $k\vec{x}_1\cdot\vec{x}_2/f$ in Eq. (11b), which are useless for the reconstruction of the object image. To avoid the phase terms, the symmetrical optical configurations (i.e., both the f-f setups or the $2f$-$2f$ setups) can be used in the test arm and the reference arm.

ACKNOWLEDGMENTS

The authors are grateful to the reviewer for his helpful comments. This work is supported by the Hi-Tech Research and Development Program of China (Grant No. 2006AA12Z115), Shanghai Fundamental Research Project (Grant No. 09JC1415000), and the National Natural Science Foundation of China (Grant No. 6087709).

[1] E. Jakeman, C. J. Oliver, and E. R. Pike, Adv. Phys. **24**, 349 (1975).
[2] S. L. Braunstein, Phys. Rev. A **42**, 474 (1990).
[3] R. J. Glauber, Phys. Rev. **130**, 2529 (1963).
[4] K. Banaszek and K. Wódkiewicz, Phys. Rev. A **55**, 3117 (1997).
[5] J. H. Shapiro and A. Shakeel, J. Opt. Soc. Am. B **14**, 232 (1997).
[6] B. Yurke, Phys. Rev. A **32**, 311 (1985).
[7] R. S. Bondurant and J. H. Shapiro, Phys. Rev. D **30**, 2548 (1984).
[8] T. B. Pittman, Y. H. Shih, D. V. Strekalov, and A. V. Sergienko, Phys. Rev. A **52**, R3429 (1995).
[9] E. Brambilla, A. Gatti, M. Bache, and L. A. Lugiato, Fortschr. Phys. **52**, 1080 (2004).
[10] M. Bache, E. Brambilla, A. Gatti, and L. A. Lugiato, Opt. Express **12**, 6067 (2004).
[11] R. S. Bennink, S. J. Bentley, and R. W. Boyd, Phys. Rev. Lett. **89**, 113601 (2002).
[12] A. Valencia, G. Scarcelli, M. D'Angelo, and Y. Shih, Phys. Rev. Lett. **94**, 063601 (2005).
[13] J. Cheng and S. Han, Phys. Rev. Lett. **92**, 093903 (2004).
[14] A. Gatti, E. Brambilla, M. Bache, and L. A. Lugiato, Phys. Rev. Lett. **93**, 093602 (2004).
[15] M. D'Angelo and Y. Shih, Laser Phys. Lett. **2**, 567 (2005).
[16] M. H. Zhang, Q. Wei, X. Shen, Y. F. Liu, and S. S. Han, Acta Opt. Sin. **27**, 1885 (2007).
[17] J. W. Goodman, *Introduction to Fourier Optics* (McGraw-Hill, New York, 1968).
[18] J. W. Goodman, *Statistical Optics* (Wiley, USA, 2000).
[19] M. Bache, E. Brambilla, A. Gatti, and L. A. Lugiato, Phys. Rev. A **70**, 023823 (2004).
[20] L. Mandel and E. Wolf, Rev. Mod. Phys. **37**, 231 (1965).
[21] E. C. G. Sudarshan, Phys. Rev. Lett. **10**, 277 (1963).